

# Advanced multi-contrast Jones matrix optical coherence tomography for Doppler and polarization sensitive imaging

Myeong Jin Ju,<sup>1,3,4</sup> Young-Joo Hong,<sup>1,4</sup> Shuichi Makita,<sup>1,4</sup> Yiheng Lim,<sup>1,4</sup> Kazuhiro Kurokawa,<sup>1,4</sup> Lian Duan,<sup>1,4</sup> Masahiro Miura,<sup>2</sup> Shuo Tang,<sup>3</sup> and Yoshiaki Yasuno<sup>1,4\*</sup>

<sup>1</sup>Computational Optics Group, University of Tsukuba, Tsukuba, Ibaraki, Japan

<sup>2</sup>Department of Ophthalmology, Ibaraki Medical Center, Tokyo Medical University, Ami, Ibaraki, Japan

<sup>3</sup>Department of Electrical and Computer Engineering, University of British Columbia, Vancouver, Canada

<sup>4</sup>Computational Optics and Ophthalmology Group, Tsukuba, Ibaraki, Japan

[\\*yasuno@optlab2.bk.tsukuba.ac.jp](mailto:*yasuno@optlab2.bk.tsukuba.ac.jp)

<http://optics.bk.tsukuba.ac.jp/COG/>

**Abstract:** An advanced version of Jones matrix optical coherence tomography (JMT) is demonstrated for Doppler and polarization sensitive imaging of the posterior eye. JMT is capable of providing localized flow tomography by Doppler detection and investigating the birefringence property of tissue through a three-dimensional (3-D) Jones matrix measurement. Owing to an incident polarization multiplexing scheme based on passive optical components, this system is stable, safe in a clinical environment, and cost effective. Since the properties of this version of JMT provide intrinsic compensation for system imperfection, the system is easy to calibrate. Compared with the previous version of JMT, this advanced JMT achieves a sufficiently long depth measurement range for clinical cases of posterior eye disease. Furthermore, a fine spectral shift compensation method based on the cross-correlation of calibration signals was devised for stabilizing the phase of OCT, which enables a high sensitivity Doppler OCT measurement. In addition, a new theory of JMT which integrates the Jones matrix measurement, Doppler measurement, and scattering measurement is presented. This theory enables a sensitivity-enhanced scattering OCT and high-sensitivity Doppler OCT. These new features enable the application of this system to clinical cases. A healthy subject and a geographic atrophy patient were measured *in vivo*, and simultaneous imaging of choroidal vasculature and birefringence structures are demonstrated.

© 2013 Optical Society of America

**OCIS codes:** (170.4500) Optical coherence tomography; (170.4460) Ophthalmic optics and devices; (170.4470) Ophthalmology; (170.3880) Medical and biological imaging; (170.3340) Laser Doppler velocimetry; (110.5405) Polarimetric imaging; (120.5410) Polarimetry; (110.4500) Optical coherence tomography.

## References and links

1. J. G. Fujimoto and W. Drexler, *Optical Coherence Tomography: Technology and Applications* (Springer, 2008).
2. S. Alam, R. J. Zawadzki, S. Choi, C. Gerth, S. S. Park, L. Morse, and J. S. Werner, "Clinical application of rapid serial fourier-domain optical coherence tomography for macular imaging," *Ophthalmology* **113**, 1425–1431 (2006).
3. V. J. Srinivasan, M. Wojtkowski, A. J. Witkin, J. S. Duker, T. H. Ko, M. Carvalho, J. S. Schuman, A. Kowalczyk, and J. G. Fujimoto, "High-definition and 3-dimensional imaging of macular pathologies with high-speed ultrahigh-resolution optical coherence tomography," *Ophthalmology* **113**, 2054.e1–2054.14 (2006). PMID: 17074565PMCID: PMC1939823.
4. M. Hangai, Y. Ojima, N. Gotoh, R. Inoue, Y. Yasuno, S. Makita, M. Yamanari, T. Yatagai, M. Kita, and N. Yoshimura, "Three-dimensional imaging of macular holes with high-speed optical coherence tomography," *Ophthalmology* **114**, 763–773 (2007). PMID: 17187861.
5. T. C. Chen, "Spectral domain optical coherence tomography in glaucoma: Qualitative and quantitative analysis of the optic nerve head and retinal nerve fiber layer (An AOS thesis)," *Trans. Am. Ophthalmol. Soc.* **107**, 254–281 (2009). PMID: 20126502PMCID: PMC2814580.
6. J. A. Izatt, M. R. Hee, E. A. Swanson, C. P. Lin, D. Huang, J. S. Schuman, C. A. Puliafito, and J. G. Fujimoto, "Micrometer-scale resolution imaging of the anterior eye in vivo with optical coherence tomography," *Arch. Ophthalmol.* **112**, 1584–1589 (1994).
7. A. R. S. Radhakrishnan, "Real-time optical coherence tomography of the anterior segment at 1310 nm," *Arch. Ophthalmol.* **119**, 1179–1185 (2001).
8. J. Welzel, E. Lankenau, R. Birngruber, and R. Engelhardt, "Optical coherence tomography of the human skin," *J. Am. Acad. Dermatol.* **37**, 958–963 (1997).
9. Y. Pan and D. L. Farkas, "Noninvasive imaging of living human skin with dual-wavelength optical coherence tomography in two and three dimensions," *J. Biomed. Opt.* **3**, 446–455 (1998).
10. P. J. Tadrous, "Methods for imaging the structure and function of living tissues and cells: 1. optical coherence tomography," *J. Pathol.* **191**, 115–119 (2000).
11. J. Welzel, "Optical coherence tomography in dermatology: a review," *Skin Res. Technol.* **7**, 1–9 (2001).
12. T. Gambichler, G. Moussa, M. Sand, D. Sand, P. Altmeyer, and K. Hoffmann, "Applications of optical coherence tomography in dermatology," *J. Dermatol. Sci.* **40**, 85–94 (2005).
13. T. Gambichler, R. Matip, G. Moussa, P. Altmeyer, and K. Hoffmann, "In vivo data of epidermal thickness evaluated by optical coherence tomography: Effects of age, gender, skin type, and anatomic site," *J. Dermatol. Sci.* **44**, 145–152 (2006).
14. V. R. Korde, G. T. Bonnema, W. Xu, C. Krishnamurthy, J. Ranger-Moore, K. Saboda, L. D. Slayton, S. J. Salasche, J. A. Warneke, D. S. Alberts, and J. K. Barton, "Using optical coherence tomography to evaluate skin sun damage and precancer," *Lasers Surg. Med.* **39**, 687–695 (2007).
15. J. Lademann, N. Otberg, H. Richter, L. Meyer, H. Audring, A. Teichmann, S. Thomas, A. Knüttel, and W. Sterry, "Application of optical non-invasive methods in skin physiology: a comparison of laser scanning microscopy and optical coherent tomography with histological analysis," *Skin Res. Technol.* **13**, 119–132 (2007).
16. B. Colston, U. Sathyam, L. DaSilva, M. Everett, P. Stroeve, and L. Otis, "Dental OCT," *Opt. Express* **3**, 230–238 (1998).
17. F. Feldchtein, V. Gelikonov, R. Iksanov, G. Gelikonov, R. Kuranov, A. Sergeev, N. Gladkova, M. Ourutina, D. Reitze, and J. Warren, "In vivo OCT imaging of hard and soft tissue of the oral cavity," *Opt. Express* **3**, 239–250 (1998).
18. B. T. Amaechi, S. M. Higham, A. G. Podoleanu, J. A. Rogers, and D. A. Jackson, "Use of optical coherence tomography for assessment of dental caries: quantitative procedure," *J. Oral Rehabil.* **28**, 1092–1093 (2001).
19. R. Brandenburg, B. Haller, and C. Hauger, "Real-time in vivo imaging of dental tissue by means of optical coherence tomography (OCT)," *Opt. Commun.* **227**, 203–211 (2003).
20. J. Izatt, M. Kulkarni, H.-W. Wang, K. Kobayashi, and J. Sivak, M.V., "Optical coherence tomography and microscopy in gastrointestinal tissues," *IEEE J. Sel. Top. Quant.* **2**, 1017–1028 (1996).
21. S. Brand, J. M. Poneroy, B. E. Bouma, G. J. Tearney, C. C. Compton, and N. S. Nishioka, "Optical coherence tomography in the gastrointestinal tract," *Endoscopy* **32**, 796–803 (2000).
22. B. Shen, G. Zuccaro Jr, T. L. Gramlich, N. Gladkova, P. Trolli, M. Kareta, C. P. Delaney, J. T. Connor, B. A. Lashner, C. L. Bevins, F. Feldchtein, F. H. Remzi, M. L. Bambrick, and V. W. Fazio, "In vivo colonoscopic optical coherence tomography for transmural inflammation in inflammatory bowel disease," *Clin. Gastroenterol. Hepatol.* **2**, 1080–1087 (2004).
23. I.-K. Jang, G. J. Tearney, B. MacNeill, M. Takano, F. Moselewski, N. Iftima, M. Shishkov, S. Houser, H. T. Aretz, E. F. Halpern, and B. E. Bouma, "In vivo characterization of coronary atherosclerotic plaque by use of optical coherence tomography," *Circulation* **111**, 1551–1555 (2005).
24. N. Gonzalo, P. W. Serruys, T. Okamura, Z. J. Shen, Y. Onuma, H. M. Garcia-Garcia, G. Sarno, C. Schultz, R. J. v. Geuns, J. Ligthart, and E. Regar, "Optical coherence tomography assessment of the acute effects of stent implantation on the vessel wall: a systematic quantitative approach," *Heart* **95**, 1913–1919 (2009).
25. F. Prati, E. Regar, G. S. Mintz, E. Arbustini, C. D. Mario, I.-K. Jang, T. Akasaka, M. Costa, G. Guagliumi,

- E. Grube, Y. Ozaki, F. Pinto, and P. W. J. Serruys, "Expert review document on methodology, terminology, and clinical applications of optical coherence tomography: physical principles, methodology of image acquisition, and clinical application for assessment of coronary arteries and atherosclerosis," *Eur. Heart J.* **31**, 401–415 (2010).
26. T. Yonetsu, T. Kakuta, T. Lee, K. Takayama, K. Kakita, T. Iwamoto, N. Kawaguchi, K. Takahashi, G. Yamamoto, Y. Iesaka, H. Fujiwara, and M. Isobe, "Assessment of acute injuries and chronic intimal thickening of the radial artery after transradial coronary intervention by optical coherence tomography," *Eur. Heart J.* **31**, 1608–1615 (2010).
  27. T. Kubo, C. Xu, Z. Wang, N. S. v. Ditzhuijzen, and H. G. Bezerra, "Plaque and thrombus evaluation by optical coherence tomography," *Int. J. Cardiovasc. Imaging* **27**, 289–298 (2011).
  28. Y. Ozaki, H. Kitabata, H. Tsujioka, S. Hosokawa, M. Kashiwagi, K. Ishibashi, K. Komukai, T. Tanimoto, Y. Ino, S. Takarada, T. Kubo, K. Kimura, A. Tanaka, K. Hirata, M. Mizukoshi, T. Imanishi, and T. Akasaka, "Comparison of contrast media and low-molecular-weight dextran for frequency-domain optical coherence tomography," *Circ. J.* **76**, 922–927 (2012).
  29. Z. Chen, T. E. Milner, D. Dave, and J. S. Nelson, "Optical doppler tomographic imaging of fluid flow velocity in highly scattering media," *Opt. Lett.* **22**, 64–66 (1997).
  30. B. R. White, M. C. Pierce, N. Nassif, B. Cense, B. H. Park, G. J. Tearney, B. E. Bouma, T. C. Chen, and J. F. de Boer, "*In vivo* dynamic human retinal blood flow imaging using ultra-high-speed spectral domain optical coherence tomography," *Opt. Express* **11**, 3490–3497 (2003).
  31. R. A. Leitgeb, L. Schmetterer, C. K. Hitzenberger, A. F. Fercher, F. Berisha, M. Wojtkowski, and T. Bajraszewski, "Real-time measurement of *in vitro* flow by fourier-domain color doppler optical coherence tomography," *Opt. Lett.* **29**, 171–173 (2004).
  32. H. Li, B. A. Standish, A. Mariampillai, N. R. Munce, Y. Mao, S. Chiu, N. E. Marcon, B. C. Wilson, A. Vitkin, and V. X. Yang, "Feasibility of interstitial doppler optical coherence tomography for *in vivo* detection of microvascular changes during photodynamic therapy," *Lasers Surg. Med.* **38**, 754–761 (2006).
  33. V. J. Srinivasan, S. Sakadžić, I. Gorczynska, S. Ruvinskaya, W. Wu, J. G. Fujimoto, and D. A. Boas, "Quantitative cerebral blood flow with optical coherence tomography," *Opt. Express* **18**, 2477 (2010).
  34. R. A. Leitgeb, L. Schmetterer, W. Drexler, A. F. Fercher, R. J. Zawadzki, and T. Bajraszewski, "Real-time assessment of retinal blood flow with ultrafast acquisition by color doppler fourier domain optical coherence tomography," *Opt. Express* **11**, 3116–3121 (2003).
  35. B. Baumann, B. Potsaid, M. F. Kraus, J. J. Liu, D. Huang, J. Hornegger, A. E. Cable, J. S. Duker, and J. G. Fujimoto, "Total retinal blood flow measurement with ultrahigh speed swept source/Fourier domain OCT," *Biomed. Opt. Express* **2**, 1539–1552 (2011).
  36. S. Makita, Y. Hong, M. Yamanari, T. Yatagai, and Y. Yasuno, "Optical coherence angiography," *Opt. Express* **14**, 7821–7840 (2006).
  37. M. R. Hee, D. Huang, E. A. Swanson, and J. G. Fujimoto, "Polarization-sensitive low-coherence reflectometer for birefringence characterization and ranging," *J. Opt. Soc. Am. B* **9**, 903–908 (1992).
  38. J. F. de Boer, T. E. Milner, M. J. C. van Gemert, and J. S. Nelson, "Two-dimensional birefringence imaging in biological tissue by polarization-sensitive optical coherence tomography," *Opt. Lett.* **22**, 934–936 (1997).
  39. Y. Yasuno, S. Makita, Y. Sutoh, M. Itoh, and T. Yatagai, "Birefringence imaging of human skin by polarization-sensitive spectral interferometric optical coherence tomography," *Opt. Lett.* **27**, 1803–1805 (2002).
  40. M. Yamanari, S. Makita, V. D. Madjarova, T. Yatagai, and Y. Yasuno, "Fiber-based polarization-sensitive fourier domain optical coherence tomography using b-scan-oriented polarization modulation method," *Opt. Express* **14**, 6502–6515 (2006).
  41. M. Yamanari, S. Makita, and Y. Yasuno, "Polarization-sensitive swept-source optical coherence tomography with continuous source polarization modulation," *Opt. Express* **16**, 5892–5906 (2008).
  42. M. Pircher, E. Götzinger, R. Leitgeb, H. Sattmann, O. Findl, and C. Hitzenberger, "Imaging of polarization properties of human retina *in vivo* with phase resolved transversal PS-OCT," *Opt. Express* **12**, 5940–5951 (2004).
  43. E. Götzinger, M. Pircher, and C. K. Hitzenberger, "High speed spectral domain polarization sensitive optical coherence tomography of the human retina," *Opt. Express* **13**, 10217–10229 (2005).
  44. M. Miura, M. Yamanari, T. Iwasaki, A. E. Elsner, S. Makita, T. Yatagai, and Y. Yasuno, "Imaging polarimetry in age-related macular degeneration," *Invest. Ophthalmol. Vis. Sci.* **49**, 2661–2667 (2008). PMID: 18515594.
  45. Y. Yasuno, M. Yamanari, K. Kawana, T. Oshika, and M. Miura, "Investigation of post-glaucoma-surgery structures by three-dimensional and polarization sensitive anterior eye segment optical coherence tomography," *Opt. Express* **17**, 3980–3996 (2009).
  46. E. Götzinger, M. Pircher, B. Baumann, C. Ahlers, W. Geitzenauer, U. Schmidt-Erfurth, and C. K. Hitzenberger, "Three-dimensional polarization sensitive OCT imaging and interactive display of the human retina," *Opt. Express* **17**, 4151–4165 (2009).
  47. M. Pircher, E. Götzinger, O. Findl, S. Michels, W. Geitzenauer, C. Leydolt, U. Schmidt-Erfurth, and C. K. Hitzenberger, "Human macula investigated *in vivo* with polarization-sensitive optical coherence tomography," *Invest. Ophthalmol. Vis. Sci.* **47**, 5487–5494 (2006). PMID: 17122140.
  48. E. Götzinger, M. Pircher, W. Geitzenauer, C. Ahlers, B. Baumann, S. Michels, U. Schmidt-Erfurth, and C. K. Hitzenberger, "Retinal pigment epithelium segmentation by polarization sensitive optical coherence tomography,"

- Opt. Express **16**, 16410–16422 (2008).
49. B. Cense, T. C. Chen, B. H. Park, M. C. Pierce, and J. F. de Boer, “Invivo depth-resolved birefringence measurements of the human retinal nerve fiber layer by polarization-sensitive optical coherence tomography,” Opt. Lett. **27**, 1610–1612 (2002).
  50. B. Cense, T. C. Chen, B. H. Park, M. C. Pierce, and J. F. de Boer, “Thickness and birefringence of healthy retinal nerve fiber layer tissue measured with polarization-sensitive optical coherence tomography,” Invest. Ophthalmol. Vis. Sci. **45**, 2606–2612 (2004). PMID: 15277483.
  51. B. Cense, M. Mujat, T. C. Chen, B. H. Park, and J. F. de Boer, “Polarization-sensitive spectral-domain optical coherence tomography using a single line scan camera,” Opt. Express **15**, 2421–2431 (2007).
  52. M. Mujat, B. H. Park, B. Cense, T. C. Chen, and J. F. de Boer, “Autocalibration of spectral-domain optical coherence tomography spectrometers for in vivo quantitative retinal nerve fiber layer birefringence determination,” J. Biomed. Opt. **12**, 041205 (2007). PMID: 17867794.
  53. M. Yamanari, M. Miura, S. Makita, T. Yatagai, and Y. Yasuno, “Phase retardation measurement of retinal nerve fiber layer by polarization-sensitive spectral-domain optical coherence tomography and scanning laser polarimetry,” J. Biomed. Opt. **13**, 014013 (2008). PMID: 18315371.
  54. E. Götzinger, M. Pircher, B. Baumann, C. Hirn, C. Vass, and C. K. Hitzenberger, “Analysis of the origin of atypical scanning laser polarimetry patterns by polarization-sensitive optical coherence tomography,” Invest. Ophthalmol. Vis. Sci. **49**, 5366–5372 (2008). PMID: 19036999.
  55. J. F. de Boer, T. E. Milner, and J. S. Nelson, “Determination of the depth-resolved stokes parameters of light backscattered from turbid media by use of polarization-sensitive optical coherence tomography,” Opt. Lett. **24**, 300–302 (1999).
  56. J. F. de Boer and T. E. Milner, “Review of polarization sensitive optical coherence tomography and stokes vector determination,” J. Biomed. Opt. **7**, 359–371 (2002).
  57. S. Jiao and L. V. Wang, “Jones-matrix imaging of biological tissues with quadruple-channel optical coherence tomography,” J. Biomed. Opt. **7**, 350–358 (2002). PMID: 12175284.
  58. S. Jiao, W. Yu, G. Stoica, and L. Wang, “Optical-fiber-based mueller optical coherence tomography,” Opt. Lett. **28**, 1206–1208 (2003).
  59. B. H. Park, M. C. Pierce, B. Cense, and J. F. de Boer, “Jones matrix analysis for a polarization-sensitive optical coherence tomography system using fiber-optic components,” Opt. Lett. **29**, 2512–2514 (2004).
  60. Y. Lim, Y.-J. Hong, L. Duan, M. Yamanari, and Y. Yasuno, “Passive component based multifunctional jones matrix swept source optical coherence tomography for doppler and polarization imaging,” Opt. Lett. **37**, 1958–1960 (2012).
  61. B. Baumann, W. Choi, B. Potsaid, D. Huang, J. S. Duker, and J. G. Fujimoto, “Swept source / fourier domain polarization sensitive optical coherence tomography with a passive polarization delay unit,” Opt. Express **20**, 10229–10241 (2012).
  62. American National Standards Institute, *American National Standard for the Safe Use of Lasers ANSI Z136.1-2007* (American National Standards Institute, New York, 2007).
  63. Y. Yasuno, V. D. Madjarova, S. Makita, M. Akiba, A. Morosawa, C. Chong, T. Sakai, K.-P. Chan, M. Itoh, and T. Yatagai, “Three-dimensional and high-speed swept-source optical coherence tomography for in vivo investigation of human anterior eye segments,” Opt. Express **13**, 10652–10664 (2005).
  64. Y. Yasuno, Y. Hong, S. Makita, M. Yamanari, M. Akiba, M. Miura, and T. Yatagai, “In vivo high-contrast imaging of deep posterior eye by 1- $\mu\text{m}$  swept source optical coherence tomography and scattering optical coherence angiography,” Opt. Express **15**, 6121–6139 (2007).
  65. B. Vakoc, S. Yun, J. de Boer, G. Tearney, and B. Bouma, “Phase-resolved optical frequency domain imaging,” Opt. Express **13**, 5483–5493 (2005).
  66. B. Braaf, K. A. Vermeer, V. A. D. Sicam, E. van Zeeburg, J. C. van Meurs, and J. F. de Boer, “Phase-stabilized optical frequency domain imaging at 1- $\mu\text{m}$  for the measurement of blood flow in the human choroid,” Opt. Express **19**, 20886–20903 (2011).
  67. Y.-J. Hong, S. Makita, F. Jaillon, M. J. Ju, E. J. Min, B. H. Lee, M. Itoh, M. Miura, and Y. Yasuno, “High-penetration swept source doppler optical coherence angiography by fully numerical phase stabilization,” Opt. Express **20**, 2740–2760 (2012).
  68. S. Makita, M. Yamanari, and Y. Yasuno, “Generalized jones matrix optical coherence tomography: performance and local birefringence imaging,” Opt. Express **18**, 854–876 (2010).
  69. M. Yamanari, S. Makita, Y. Lim, and Y. Yasuno, “Full-range polarization-sensitive swept-source optical coherence tomography by simultaneous transversal and spectral modulation,” Opt. Express **18**, 13964–13980 (2010).
  70. Y. Lim, M. Yamanari, S. Fukuda, Y. Kaji, T. Kiuchi, M. Miura, T. Oshika, and Y. Yasuno, “Birefringence measurement of cornea and anterior segment by office-based polarization-sensitive optical coherence tomography,” Biomed. Opt. Express **2**, 2392–2402 (2011).
  71. B. J. Vakoc, R. M. Lanning, J. A. Tyrrell, T. P. Padera, L. A. Bartlett, T. Stylianopoulos, L. L. Munn, G. J. Tearney, D. Fukumura, R. K. Jain, and B. E. Bouma, “Three-dimensional microscopy of the tumor microenvironment in vivo using optical frequency domain imaging,” Nat. Med. **15**, 1219–1223 (2009).
  72. K. Kurokawa, K. Sasaki, S. Makita, Y.-J. Hong, and Y. Yasuno, “Three-dimensional retinal and choroidal cap-

- illary imaging by power doppler optical coherence angiography with adaptive optics," *Opt. Express* **20**, 22796–22812 (2012).
73. J. P. Sarks, S. H. Sarks, and M. C. Killingsworth, "Evolution of geographic atrophy of the retinal pigment epithelium," *Eye* **2**, 552–577 (1988). PMID: 2476333.
  74. R. Klein, M. D. Davis, Y. L. Magli, P. Segal, B. E. Klein, and L. Hubbard, "The wisconsin age-related maculopathy grading system," *Ophthalmology* **98**, 1128–1134 (1991). PMID: 1843453.
  75. J. J. Weiter, F. C. Delori, G. L. Wing, and K. A. Fitch, "Retinal pigment epithelial lipofuscin and melanin and choroidal melanin in human eyes." *Invest. Ophthalmol. Vis. Sci.* **27**, 145–152 (1986).
  76. S. Moon, S.-W. Lee, and Z. Chen, "Reference spectrum extraction and fixed-pattern noise removal in optical coherence tomography," *Opt. Express* **18**, 24395–24404 (2010).
- 

## 1. Introduction

Optical coherence tomography (OCT) [1] is a non-invasive and high-contrast imaging modality that is capable of visualizing a cross-sectional and three-dimensional structure of biological tissue at a micrometer resolution of around 2 to 15  $\mu\text{m}$ . OCT has been widely applied for ophthalmology [2–7], dermatology [8–15], dentistry [16–19], gastroenterology [20–22], and cardiology [23–28].

Through several extensions of function, clinical applications and the potential of OCT techniques have been discovered and enhanced. Doppler OCT [29–31] has been developed and applied for clinical and biological investigations, such as cancer imaging [32], brain imaging [33], and ophthalmic investigation [34, 35]. Optical coherence angiography (OCA) [36] was a variation of Doppler OCT and is for visualizing retinal and choroidal vasculatures in detail, comparable to the conventional angiographic methods such as Fluorescein angiography (FA) and indocyanine green angiography (ICGA) in terms of vasculature imaging.

As another example of a functional extension of OCT, polarization-sensitive OCT (PS-OCT), which is capable of measuring the birefringence of a tissue, has been developed [37–41]. PS-OCT has also been applied to ophthalmic imaging for providing additional contrast to fibrous tissues [42–46], retinal pigment epithelium (RPE) [47, 48], and for performing a quantitative assessment of nerve fibers [49–54].

Jones-matrix-based OCT (Jones matrix OCT) [40, 41, 55–59] has been developed as one of the several sub-types of PS-OCTs. Recently, a passive-component-based Jones matrix OCT system was independently demonstrated by the authors [60] and Baumann et al. [61]. This system realized Jones matrix measurements without any active modulation devices, e.g. electro-optic or acousto-optic modulators. In particular, a fiber-based multi-contrast Jones matrix swept-source OCT [60] was used for simultaneous Doppler and polarization imaging. For measuring both a standard wave plate and a retina of a healthy subject *in vivo*, accuracy of the polarization detection and its functionality was verified. Because of the depth-encoded polarization multiplexing method, however, the measurable depth range was relatively shorter than that of a non-polarization OCT system. Furthermore, its phase instability and relatively low imaging quality limit the system for clinical applications.

In the presented study, advanced multi-contrast Jones matrix OCT (MC-JMT) is demonstrated. In comparison to our previous MC-JMT [60], this new MC-JMT is advanced in terms of phase stability, image quality, and imaging depth. In addition, this advanced MC-JMT is based on a new principle in which all of the measurements of scattering OCT, Doppler OCT and PS-OCT are integrated. Distinct features of the system and post-processing algorithms are also concretely described. Furthermore we show the measurement results of a healthy and clinical case subject, demonstrating the utility of the system for clinical ophthalmology.

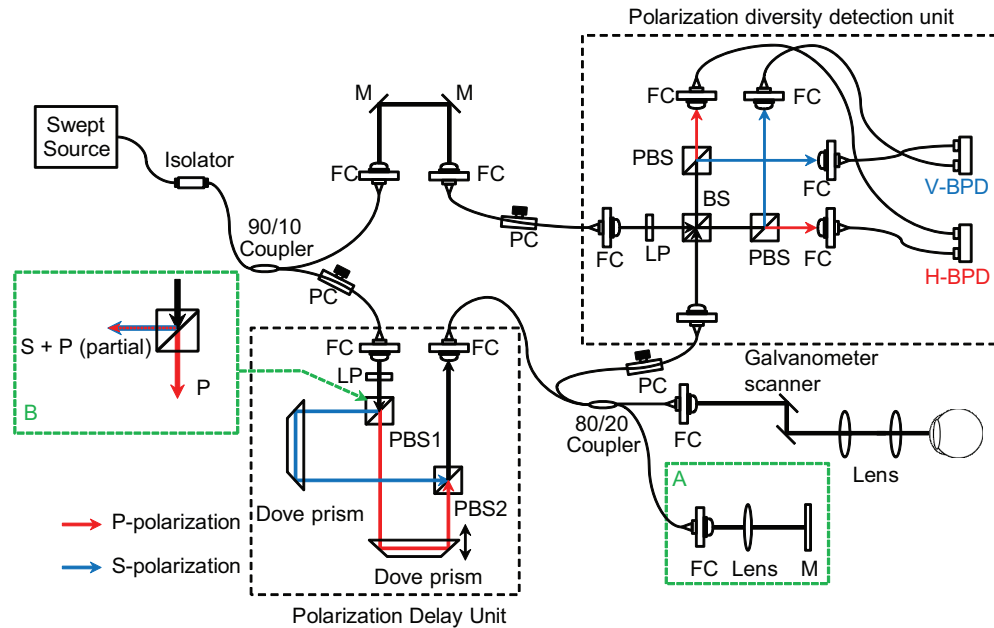


Fig. 1. Schematic diagram of MC-JMT system. LP: linear polarizer, PC: polarization controller, FC: fiber collimator, M: mirror, PBS: polarizing beam splitter, BS: beam splitter, H- and V-BPD: balanced photo-detector for horizontally and vertically polarized signals, respectively.

## 2. Multi-contrast Jones matrix tomography

### 2.1. System configuration

Figure 1 shows the schematic of MC-JMT system. An MEMS-based swept-source (Axsun Technology Inc., MA) with a center wavelength of  $1.06 \mu\text{m}$ , full width at half maximum (FWHM) of 111 nm, and scanning width of 123 nm was used as a light source. The scanning rate of the light source is 100 kHz, and the average output power is 30 mW.

The interferometer is built with single-mode optical fibers. The light is split by a 90:10 single-mode optical fiber coupler after passing through an isolator used for the protection of the source from back-reflected lights. The 90% port of the fiber coupler is connected to a probe arm consisting of a polarization controller and a passive polarization delay unit, described in Section 2.2. The 10% portion of the light from the coupler is coupled to a reference arm.

The light from the polarization delay unit passes through an 80:20 fiber coupler. The 80% portion of the light is directed to a calibration reflector (box-A in Fig. 1) composed of a fiber collimator, lens, and mirror, and the remaining 20% portion of the light illuminates the eye after passing through a collimator (F280 APC-C, Thorlabs Inc., NJ), a two-axis galvanometer scanner, an objective lens ( $f = 60 \text{ mm}$ ), and an aspheric ophthalmic lens (40D, Volk Optical Inc., OH). The beam diameter incident on the cornea and spot size at a retina are around 1.4 mm and  $21 \mu\text{m}$ , respectively. The optical power on the cornea is configured to be around 1.15 mW in order to satisfy the safety standard defined by ANSI [62]. The back-scattered light from the retina is recoupled to the 80:20 coupler, and 80% of the back-scattered light is directed to a polarization diversity (PD) detection unit.

The PD detection unit consists of a linear polarizer, a non-polarizing beam splitter (BS), two polarizing beam splitters (PBSs), and two 350 MHz balanced photo-detectors (BPDs),

PDB430C, Thorlabs Inc.). The reference light coupled through the 90:10 fiber coupler is also directed to the PD detection unit, in which a linear polarizer is embedded for aligning the polarization state of the light to 45-degree angle. In the PD detection unit, the reference and back-scattered light from the eye is combined at the BS, split into horizontal and vertical polarization components by the two PBSs, and finally detected by the BPDs. The detected signals from the BPDs were sampled by an ATS9350 digitizer (AlazarTech Inc., Pointe Claire, QC, Canada) with 12-bit resolution and a sampling rate of 500 MHz after passing through a high-pass (1.5 MHz) and low-pass (250 MHz) filter (HP1CH3-0S and LP250Ch3-0S, R&K Co. Ltd., Shizuoka, Japan). Here the interference signal was sampled with 2560 sampling points and the effective wavelength range being sampled was approximately 110 nm. The sampled interference signals were rescaled to the linear frequency domain using pre-defined rescaling parameters determined by a time-frequency calibration method [63]. The rescaling algorithm also cancels the spectral shift among A-lines and stabilizes the phase of the OCT signal as described in Section 3.1. After applying a Gaussian window, the interference signal was Fourier transformed to yield an OCT signal. For the retinal measurement, the chromatic dispersion of the eye as well as the residual dispersion of the interferometer is canceled by a method described in Section 2.3 of Ref. 64. The scanning property of the light source, the parameters for the sampling of the spectral interference signal, and the windowing finally define the measured depth-resolution of 8.5  $\mu\text{m}$  in air, corresponding to 6.2  $\mu\text{m}$  in tissue.

With an average probe power of 1.15 mW, the sensitivity was to be 91.05 dB and the signal roll-off measured at 0.3 to 2.6-mm depth range was -0.65 dB/mm. Because the signal energy is split into the four OCT images, the sensitivity of the system measured for a single image is 6-dB lower than that of standard OCT. This fundamental sensitivity loss is going to be overcome by a method discussed in Section 3.6. By accounting the fundamental loss of the 80:20 coupler, the shot-noise-limited sensitivity of a single image becomes -99.4 dB. The departure of the measured sensitivity from the shot-noise-limited sensitivity of -8.4 dB is accounted by the double-pass transmittance of the posterior-eye-scanning unit, which has been measured to be -3.8 dB, the fiber-coupling loss at the PD detection unit, which has been measured to be -3.7 dB and possible recoupling loss at the fiber-tip in the scanning unit occurred by the misalignment of a mirror target for the sensitivity measurement.

## 2.2. Incident polarization multiplexing by polarization delay unit

A passive polarization delay unit is used to multiplex two incident polarization states by applying the optical path lengths difference (OPLD). As shown in Fig. 1, the passive polarization delay unit consists of a linear polarizer, two PBSs, and two Dove prisms. In this delay unit, the collimated light is passing through a linear polarizer oriented at 45-degree angle and split into two orthogonal polarization components by the PBS 1. After the internal reflection in the Dove prisms, the two orthogonally polarized lights are combined by the PBS 2, then coupled to an optical fiber connected to the 80:20 fiber coupler.

The two incident polarization states are multiplexed in depth position, and the OPLD is adjusted by moving one of the Dove prisms. In our particular setup, the OPLD is adjusted to  $z_d = 3.1$  mm, so two OCT signals corresponding to the two multiplexed incident polarization states appear with a depth separation of 3.1 mm. With this configuration, the measurable imaging depth range for each signal was determined to be around 2.95 mm, which is large enough for clinical imaging of pathologic posterior eyes.

Since this polarization delay unit is compact in size and consists only of bulk optical components, the perturbation of the delay caused by temperature fluctuation is negligible. In addition, this polarization delay unit relies only on passive polarization components. This results in high stability and easy operation of the MC-JMT.

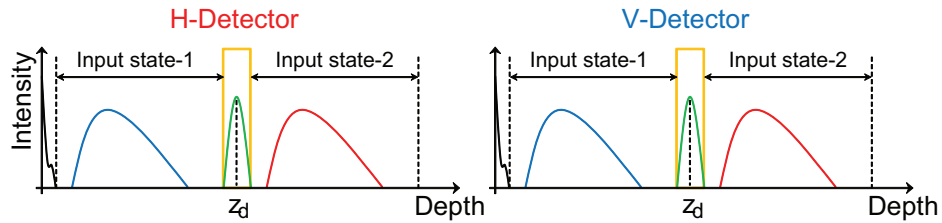


Fig. 2. Diagram of the Fourier transformed interference signals from horizontal (H) and vertical (V) detection channels.

### 2.3. Polarization diversity detection

MC-JMT relies on PD detection, by which two interference signals corresponding to different polarization states are independently detected. It should be noted that the two polarization states are not necessarily identical to those of the polarization delay unit. By this detection scheme, two interference signals of different polarization states are simultaneously detected by two balanced photodetectors. Each interference signal generates two OCT images at different depth positions, which correspond to the two incident polarization states multiplexed by the polarization delay unit. Finally, owing to the PD detection and the incident polarization multiplexing, four OCT images are simultaneously acquired as schematically shown in Fig. 2.

### 2.4. Phase calibration reflector

In this MC-JMT, the fluctuations in spectral sampling timing among OCT A-lines are monitored and canceled using a stable spectral interference fringe denoted as a calibration signal. The generation of a calibration signal relies on the imperfection of the PBSs in the polarization delay unit. Ideally, the PBS separates S- and P-polarization components by reflecting only the S-polarization component and transmitting only the P-polarization component. However, with an off-the-shelf PBS, some portion of the P-polarization component is reflected and mixed with the S-polarization component. At the 1.06- $\mu\text{m}$  wavelength, according to the manufacturer's specifications, the reflected beam of the PBS employed in the passive polarization delay unit (NT49-870, Edmund Optics Inc., NJ, US) includes 4.4% of P-polarization.

Owing to this imperfection of the PBS, the polarization delay unit behaves as a Mach-Zehnder interferometer with an OPLD of  $z_d$  for the P-polarization component and generates the calibration signal. The calibration signal is directed to the BPDs in the PD detection unit through the 80:20 fiber coupler and a calibration reflector (box-A in Fig. 1). Note that the calibration signal generated by the polarization delay unit is a common-mode signal for the BPDs. However, the optical power of the calibration signal is significantly larger than that of OCT signal, and hence it can be detected even with the common-mode-rejection property of the BPD.

As shown in the orange squares in Fig. 2, the calibration signal appears at the depth location of  $z_d$  that was exactly the axial displacement between the two depth-multiplexed signals. This calibration signal is used to correct the fluctuation of spectral sampling as described in Section 3.1.

It should be noted that the imperfection of the PBS does not disturb the polarization sensitive measurement of MC-JMT. The details are discussed in Section 3.2.

### 3. Post-processing

#### 3.1. Monitoring and correction of spectral shift

Fluctuations in the synchronization between the wavelength sweeping of the light source and the digitizer causes random shifts of the digitized spectrum among the A-lines, which result in phase instability. The phase instability could impose errors on the phase measurements and degrades the sensitivity of Doppler OCT measurements. In addition, phase instability results in reduced performance of numerical cancellation of fixed pattern noise. Hence, the spectral shift should be correctly estimated and canceled. In previous systems, the spectral shift was corrected by several means [35, 41, 65–67]. In current MC-JMT, we utilize a new method specialized for the MC-JMT which is simple in its hardware configuration.

To obtain phase-stabilized OCT, the spectral shift is estimated and canceled using the calibration signal described in Section 2.4. Since the same amount of spectral shift occurs in both detection channels of the PD detection, the calibration signal with the higher signal-to-noise ratio is used to estimate the spectral shifts of both channels.

The details of the estimation of the spectral shift are as follows. In this estimation, the relative shift between the two spectra are obtained. One of the two spectra is denoted as a reference spectrum, and is typically the first A-line of a B-scan. The other spectrum is the spectrum under shift correction and its shift is corrected with respect to the reference spectrum. For the estimation, two of the digitized spectra are first Fourier transformed without rescaling. After this Fourier transform, the calibration signals appear between two OCT signals of two incident polarization components as shown in Fig. 2 (green signals) and are selected by a binary window function.

For an intuitive understanding of the method, we consider the inversely Fourier transformed spectra of the windowed calibrated signals of the reference spectrum ( $I_r(j)$ ) and the spectrum under shift-correction ( $I_c(j)$ ). These spectra are described as

$$I_r(j) = |E_r(j) + E_t(j)|^2 \quad (1)$$

$$I_c(j) = |E_r(j - \beta_j) + E_t(j - \beta_j)|^2 = I_r(j) * \delta(j - \beta_j) \quad (2)$$

where  $E_r(j)$  and  $E_t(j)$  are the sampled spectra of the reflected and transmitted beams of the polarization delay unit with a spectral sampling index of  $j$ .  $*$  denotes the convolution operation, and  $\beta_j$  indicates the relative shift of the spectrum in the number of sampling points.

In the spectral shift estimation process, the numerically Fourier transformed calibration signal of the reference A-line is multiplied with the complex conjugate of the Fourier transformed calibration signal of the A-line under correction as

$$\mathcal{F}[I_r(j)] \mathcal{F}[I_c(j)]^* = \mathcal{F}[I_r(j)] \mathcal{F}[I_r^*(-j)] \mathcal{F}[\delta(-j - \beta_j)] \quad (3)$$

where  $\mathcal{F}[\ ]$  represents the Fourier transform and the superscript of  $*$  represents the complex conjugate.

The numerical inverse Fourier transform of the signal represented by Eq. (3) yields

$$\begin{aligned} \mathcal{F}^{-1}[\mathcal{F}[I_r(j)] \mathcal{F}[I_c(j)]^*] &= I_r(j) * I_r^*(-j) * \delta(-j - \beta_j) \\ &= \{I_r(j) \otimes I_r(j)\} * \delta(-j - \beta_j) \end{aligned} \quad (4)$$

where  $\otimes$  represents the correlation operation.  $I_r(j) \otimes I_r(j)$  is the auto-correlation of  $I_r(j)$ . It would have a maximum at  $j = 0$ , so the signal represented by Eq. (4) has its maximum at  $j = -\beta_j$ . Finally, the amount of spectral shift  $\beta_j$  is determined by detecting the peak of this signal. It is noteworthy that the accuracy of the spectral shift estimation can be enhanced by

zero-padding the signal of Eq. (3). In our particular case the sampling number of the spectrum is zero-padded to yield a sampling number 16-times larger than the original, thus the spectral shift is determined with an accuracy of 1/16 of the original spectral sampling period.

The estimated  $\beta_j$  is then added to the predetermined rescaling table, which is a vector of sub-fractional indexes of spectral sampling points for each rescaled sampling point. The A-line under correction is then rescaled using this modified rescaling table and a shift-corrected and rescaled spectrum is obtained.

In the spectral estimation method described in this section, the sampled spectra are Fourier transformed without being rescaled into a linear frequency domain. And hence the calibration signal have a broad width after the Fourier transformation, which is typically around 70-pixels width, and sometimes overlaps with an interference signal originated from the sample. However, due to the significantly higher SNR of the calibration signal with respect to those of the sample signal, the calibration signal still overwhelmingly dominates the spectral shift estimation. As a result, this estimation method shows remarkable performance as discussed in Section 5.1.

### 3.2. Principle of Jones matrix OCT

Prior to examining the detailed processing algorithms of the MC-JMT, a conceptual principle for a JMT is described in this section. By employing two incident polarization states and PD detection, Jones matrix OCT determines the polarization property of a sample through Jones matrix analysis [59, 68].

By denoting the Jones vector of one of the incident polarization states as  $\vec{E}_{in}^{(1)} = [H_{in}^{(1)} \quad V_{in}^{(1)}]^T$  and the corresponding OCT signals measured by the two detectors in the PD detection unit as  $E_{outA}^{(1)}(z)$ ,  $E_{outB}^{(1)}(z)$ , and  $\vec{E}_{out}^{(1)}(z) \equiv [E_{outA}^{(1)}(z) \quad E_{outB}^{(1)}(z)]^T$ , the relationship between  $\vec{E}_{in}^{(1)}$  and  $\vec{E}_{out}^{(1)}(z)$  becomes

$$\vec{E}_{out}^{(1)}(z) = \chi \mathbf{J}_{all}(z) \vec{E}_{in}^{(1)} \quad (5)$$

where  $\mathbf{J}_{all}(z)$  is the Jones matrix representing the overall polarization property from the output point of the polarization delay unit to the PD detection unit, including the Jones matrix of the OCT system and the depth-resolved round trip Jones matrix of the sample.  $\chi$  is a general transform matrix which transforms the horizontal and vertical components of the Jones vector at the PD detection unit to the two arbitrary polarization components detected by the two detectors in the PD detection unit. In short,  $\chi$  represents the imperfection of the PD detection. This includes the imbalance in the reference power of OCT detection, the gain imbalance of the photo-detectors, and the cross-talk between the two detectors. Similarly, the other incident polarization component and its corresponding OCT signals are related as

$$\vec{E}_{out}^{(2)}(z) = \chi \mathbf{J}_{all}(z) \vec{E}_{in}^{(2)}. \quad (6)$$

Note that, in the Jones matrix OCT, using a polarization-delay-based multiplexing scheme, the OCT signals corresponding to  $\vec{E}_{in}^{(1)}(z)$  and  $\vec{E}_{in}^{(2)}(z)$  appear at two different depths. To avoid confusion, we define the variable  $z$  as the relative depth from each zero-delay point of each incident polarization component. Namely, equal values of  $z$  represent the same depth location in the sample.

Equations (5) and (6) can be combined as

$$\mathbf{E}_{out}(z) = \chi \mathbf{J}_{all}(z) \mathbf{E}_{in} \quad (7)$$

where  $\mathbf{E}_{in} \equiv \begin{bmatrix} H_{in}^{(1)} & H_{in}^{(2)} \\ V_{in}^{(1)} & V_{in}^{(2)} \end{bmatrix}$  and  $\mathbf{E}_{out}(z)$  is a matrix of measured OCT signals

$$\mathbf{E}_{out}(z) = \begin{bmatrix} E_{outA}^{(1)}(z) & E_{outA}^{(2)}(z) \\ E_{outB}^{(1)}(z) & E_{outB}^{(2)}(z) \end{bmatrix}. \quad (8)$$

Note that, in Eq. (7),  $\mathbf{E}_{out}(z)$  is a measured value, while  $\mathbf{E}_{in}$  is a predefined but not accurately known matrix.

By considering the general configuration of the Jones matrix OCT,  $\mathbf{J}_{all}(z)$  can be decomposed into three components as

$$\mathbf{J}_{all}(z) = \mathbf{J}_{out} \mathbf{J}_s(z) \mathbf{J}_{in} \quad (9)$$

where  $\mathbf{J}_{in}$  is the Jones matrix from the polarization delay unit to the sample surface,  $\mathbf{J}_{out}$  is from the sample surface to the PD detection unit, and  $\mathbf{J}_s(z) = \mathbf{J}'_s(z)^T \mathbf{J}'_s(z)$  is the round trip Jones matrix of the sample with that of a single trip being  $\mathbf{J}'_s(z)$ .

The purpose of the Jones matrix OCT measurement is to determine polarization properties of  $\mathbf{J}_s$  through its eigenvalues. To obtain the eigenvalues, a similar matrix of  $\mathbf{J}_s$  is obtained by the following protocol. First, the surface of the sample is segmented, and  $\mathbf{E}_{out}$  is obtained at the sample surface as  $\mathbf{E}_{out}(z_0)$ , where  $z_0$  represents the depth position of the surface. Then, a similar matrix of the  $\mathbf{J}_s(z)$  at each location in the sample is obtained as

$$\begin{aligned} \mathbf{E}_{out}(z) \mathbf{E}_{out}(z_0)^{-1} &= \chi \mathbf{J}_{out} \mathbf{J}_s(z) \mathbf{J}_{in} \mathbf{E}_{in} \mathbf{E}_{in}^{-1} \mathbf{J}_{in}^{-1} \mathbf{J}_{out}^{-1} \chi^{-1} \\ &= \chi \mathbf{J}_{out} \mathbf{J}_s(z) \mathbf{J}_{out}^{-1} \chi^{-1} \end{aligned} \quad (10)$$

This equation indicates that using the two measured matrices  $\mathbf{E}_{out}(z)$  and  $\mathbf{E}_{out}(z_0)$ , we can define the similar matrix of the round trip Jones matrix of the sample and hence its eigenvalues. It is noteworthy that MC-JMT provides the similar matrices regardless of the combination of the input polarization states, except when the two states are parallel to each other [68]. Owing to this inherent robustness, the imperfection of PBS, which has been used to generate the calibration signal (see Section 2.4), does not affect the polarization measurement.

In practical implementation,  $\mathbf{E}_{out}(z_0)$  is obtained by averaging the Jones matrices at the surface of the sample within a B-scan using the adaptive Jones matrix averaging method described in Section 3.4. This averaging enhances the signal-to-noise ratio (SNR) of  $\mathbf{E}_{out}(z_0)$  and provides a more reliable result.

### 3.3. Phase retardation and relative attenuation calculation

The round-trip phase retardation of the sample is obtained from the similar matrix obtained through Eq. (10). The eigenvalues of the round-trip sample Jones matrix can be obtained through matrix diagonalization [40] or the following equation [69]

$$\lambda_{1,2} = T/2 \pm \sqrt{T^2/4 - D} \quad (11)$$

where  $T$  and  $D$  are the trace and determinant of the similar matrix, and  $\lambda_{1,2}$  indicates the two eigenvalues of the matrix. Here we have utilized the fact that the eigenvalues of the similar matrix are identical to those of the round-trip Jones matrix of the sample.

The phase retardation  $\delta(z)$  is then obtained as the phase difference between two eigenvalues as

$$\delta(z) = \begin{cases} \text{Arg}[\lambda_1 \lambda_2^*] & : 0 \leq \text{Arg}[\lambda_1 \lambda_2^*] \leq \pi \\ \text{Arg}[\lambda_1^* \lambda_2] & : \text{otherwise} \end{cases}. \quad (12)$$

Note that  $\delta(z)$  is defined to be aliased into the range of  $[0, \pi]$  because the assignment of  $\lambda_1$  and  $\lambda_2$  is underspecified.

In addition to the phase retardation, the relative attenuation between two characteristic polarization states  $\varepsilon(z)$  is obtained as

$$\varepsilon(z) = \left| \ln \frac{|\lambda_1|}{|\lambda_2|} \right| \quad (13)$$

### 3.4. Adaptive Jones matrix averaging

To obtain a high quality phase retardation image, adaptive Jones matrix averaging can optionally be applied to the similar Jones matrices. Note that the basic concept of adaptive Jones matrix averaging was firstly described in Section 2.1.2 of Ref. 70 and was previously called as complex Jones averaging.

This method relies on a weighted least-square estimation of the relative global phase of a Jones matrix in respect to an arbitrary reference Jones matrix. Consider several Jones matrices  $\mathbf{M}^{(j)}$  (or similarly several of  $\mathbf{E}_{out}$ ) obtained in a single homogeneous birefringence domain of a sample but not within a coherence volume, i.e. the resolution of OCT. Under this condition, it would be rational to assume the following relationship;  $\mathbf{M}^{(0)} \simeq \exp(i\Delta\varphi^{(0,j)})\mathbf{M}^{(j)}$ . Here  $\Delta\varphi^{(0,j)}$  is the relative global phase between  $\mathbf{M}^{(0)}$  and  $\mathbf{M}^{(j)}$ . The basic concept of adaptive Jones matrix averaging is averaging  $\mathbf{M}^{(j)}$  after canceling the global phase.

In the adaptive Jones matrix averaging method, the global phase between two Jones matrices is estimated as

$$\Delta\varphi^{(0,j)} \equiv \text{Arg} \left[ \sum_{l=1}^4 \frac{\exp i \left( \text{Arg} \left[ \frac{M_l^{(j)}}{M_l^{(0)}} \right] \right)}{|M_l^{(0)}|^{-1} + |M_l^{(j)}|^{-1}} \right], \quad (14)$$

where  $M_l^{(j)}$  is the  $l$ -th entry of the  $j$ -th matrix under averaging.

After determining the global phase, the averaged matrix is defined as

$$\bar{\mathbf{M}} \equiv \sum_j \exp(-i\Delta\varphi^{(0,j)})\mathbf{M}^{(j)}. \quad (15)$$

Note that  $\mathbf{M}^{(0)}$  is a reference matrix for the determination of the global phase. Hence the phase noise of this matrix should be small. In practical processing, the Jones matrix possessing the highest total signal energy among the matrices being averaged is utilized as  $\mathbf{M}^{(0)}$ .

In practical MC-JMT measurement, this adaptive Jones matrix averaging is optionally applied to the similar matrices ( $\mathbf{E}_{out}(z)\mathbf{E}_{out}(z_0)^{-1}$ ) with an averaging kernel smaller than the birefringence domain of the sample prior to calculating the eigenvalues.

### 3.5. Degree of polarization uniformity calculation

Degree of polarization uniformity (DOPU) is a parameter originally introduced by Götzinger *et al.* [48] for representing the spatial uniformity of polarization. Since some important tissues such as retinal pigment epithelium (RPE) are selectively visualized by DOPU contrast, DOPU imaging by MC-JMT is of great interest.

DOPU was first defined by using the Hee-Hitzenberger type PS-OCT [37] and recently applied for Jones matrix OCT [61]. In our MC-JMT, DOPU is obtained directly from  $\mathbf{E}_{out}(z)$  by the following method.

Since DOPU is defined based on the Stokes parameters of back-scattered light, we should define a virtual incident beam with an arbitrary state of polarization. To simplify computation,

we assumed a virtual incident polarization state of  $\mathbf{E}_{out}(z_0)[1 \ 0]^T$ . When this virtual incident light illuminates the similar matrix of the round-trip Jones matrix,  $\mathbf{E}_{out}(z)\mathbf{E}_{out}(z_0)^{-1}$ , the Jones vector of the output light becomes  $\mathbf{E}_{out}(z)[1 \ 0]^T = \begin{bmatrix} E_{outA}^{(1)}(z) & E_{outB}^{(1)}(z) \end{bmatrix}^T$ . The corresponding Stokes parameters are then defined as

$$\mathbf{S} = \begin{bmatrix} I \\ Q \\ U \\ V \end{bmatrix} = \begin{bmatrix} |E_{outA}^{(1)}(z)|^2 + |E_{outB}^{(1)}(z)|^2 \\ |E_{outA}^{(1)}(z)|^2 - |E_{outB}^{(1)}(z)|^2 \\ E_{outA}^{(1)}(z)E_{outB}^{(1)*}(z) + E_{outA}^{(1)*}(z)E_{outB}^{(1)}(z) \\ i(E_{outA}^{(1)}(z)E_{outB}^{(1)*}(z) - E_{outA}^{(1)*}(z)E_{outB}^{(1)}(z)) \end{bmatrix} \quad (16)$$

Note that these Stokes parameters are only calculated from two OCT signals obtained from the PD detection unit.

DOPU is then defined as

$$\text{DOPU} = \sqrt{\bar{Q}^2 + \bar{U}^2 + \bar{V}^2} \quad (17)$$

with

$$(\bar{Q}, \bar{U}, \bar{V}) = \left( \sum_i \frac{Q_i}{I_i}, \sum_i \frac{U_i}{I_i}, \sum_i \frac{V_i}{I_i} \right) \quad (18)$$

where  $i$  indicates the  $i$ -th pixel within a spatial kernel by which DOPU is defined. It should be noted that this DOPU was not directly determined from the polarization property of the sample  $\mathbf{J}_s(z)$ , but from  $\mathbf{E}_{out}(z) = \chi \mathbf{J}_{out} \mathbf{J}_s(z) \mathbf{J}_{in} \mathbf{E}_{in}$ . However, it would provide a reasonable measure of the sample's DOPU, because  $\chi$ ,  $\mathbf{J}_{out}$ ,  $\mathbf{J}_{in}$ , and  $\mathbf{E}_{in}$  can be regarded as constant in space and time.

In our particular implementation, a kernel size of 8 pixels (horizontal)  $\times$  3 pixels (vertical) ( $70 \mu\text{m} \times 12 \mu\text{m}$ ) is used.

### 3.6. Coherent composition of matrix entries

In previous multi-contrast OCT based on Jones matrix OCT, a scattering OCT image was obtained by averaging the four entries of a Jones matrix in squared intensity. Similarly, Doppler tomography was obtained by averaging the squared power of the four Doppler phase shift signals of the four entries of the Jones matrix [60]. Although this method provided satisfactory image quality, it still suffered fundamental sensitivity degradation of Jones matrix OCT, caused by splitting a probe beam power into four OCT images, i.e. the four entries of the Jones matrices.

To overcome this issue, we introduced a new advanced signal processing method by which the four entries of a matrix were coherently combined. In the current advanced MC-JMT, a sensitivity-enhanced scattering OCT and Doppler OCT are obtained from a coherent composite of the four entries.

The coherent composition of the matrix entries is based on the following mathematical model of the depth resolved OCT matrix  $\mathbf{E}_{out}(z)$ .

$$\mathbf{E}_{out}(z) = \begin{bmatrix} E_{outA}^{(1)}(z) & E_{outA}^{(2)}(z) \\ E_{outB}^{(1)}(z) & E_{outB}^{(2)}(z) \end{bmatrix} \simeq \begin{bmatrix} E_{outA}^{(1)}(z) & e^{i\theta_1} E_{outA}^{(1)}(z) \\ e^{i\theta_2} E_{outA}^{(1)}(z) & e^{i\theta_3} E_{outA}^{(1)}(z) \end{bmatrix} \quad (19)$$

where  $\theta_{1,2,3}$  are depth-independent relative phase offsets with respect to the first entry. We have assumed that the birefringence of the sample is negligible, as is assumed for conventional non-polarization sensitive OCT.

In our coherent composition method,  $\theta_{1,2,3}$  are estimated as

$$\theta_1 \equiv \text{Arg} \left[ \sum_z E_{outA}^{(2)}(z) E_{outA}^{(1)}(z)^* \right] \quad (20)$$

$$\theta_2 \equiv \text{Arg} \left[ \sum_z E_{outB}^{(1)}(z) E_{outA}^{(1)}(z)^* \right] \quad (21)$$

$$\theta_3 \equiv \text{Arg} \left[ \sum_z E_{outB}^{(2)}(z) E_{outA}^{(1)}(z)^* \right] \quad (22)$$

where  $\sum_z$  represents a summation of all pixels along the depth.

Using  $\theta_{1,2,3}$ , the coherent composition is defined as

$$\overline{E_{out}}(z) = \frac{1}{4} \left[ E_{outA}^{(1)}(z) + e^{-i\theta_1} E_{outA}^{(2)}(z) + e^{-i\theta_2} E_{outB}^{(1)}(z) + e^{-i\theta_3} E_{outB}^{(2)}(z) \right]. \quad (23)$$

Since this composite signal is a coherent summation of four OCT signals, this method provides enhanced sensitivity and higher accuracy for Doppler phase shift measurement.

### 3.7. Doppler phase shift calculation

In our measurement protocol, the Doppler phase shift was defined as the phase difference between B-scans [36, 71], and for this purpose, a single location of a sample is scanned multiple times.

In general, a raw Doppler phase shift obtained from a living sample is expressed as

$$\Delta\phi(z) = \frac{4\pi\tau}{\lambda_c} n v_z(z) + \phi_b \quad (24)$$

where  $\lambda_c$  is the center wavelength,  $n$  is the refractive index of the sample,  $v_z$  is an axial velocity of the flow of interest, and  $\phi_b$  is a constant phase offset incurred by the bulk motion of the sample.  $\tau$  is a time interval between two A-scans under Doppler calculation, and, in our protocol, is equivalent to the time interval of B-scans.

In MC-JMT, the raw Doppler phase shift  $\Delta\phi(j)$  is, in principle, defined using the coherently composite signals as

$$\Delta\phi(z, j) = \text{Arg} \left[ \overline{E_{out}}(z, j+1) \overline{E_{out}}(z, j)^* \right] \quad (25)$$

where  $\Delta\phi(j)$  is the Doppler phase shift of an A-line in the  $j$ -th B-scan against the corresponding A-line in the  $(j+1)$ -th B-scan. The bulk phase offset  $\phi_b(j)$  is obtained by averaging the complex part of Eq. (25) as [72]

$$\phi_b(j) = \text{Arg} \left[ \sum_z \overline{E_{out}}(z, j+1) \overline{E_{out}}(z, j)^* \right] \quad (26)$$

where  $j$  denotes the index of the B-scan.

In our measurement protocol, multiple ( $m$ ) B-scans are obtained at the same location of a sample. Using these  $m$  B-scans and their bulk phase offsets, a sensitivity-enhanced Doppler signal is obtained as

$$\overline{\Delta\phi}(z, j) = \text{Arg} \left[ \sum_{j=m_0}^{m_0+m-2} \overline{E_{out}}(z, j+1) \overline{E_{out}}(z, j)^* \exp(-i\phi_b(j)) W(z, j) \right] \quad (27)$$

where  $m_0$  is the starting B-scan index of the multiple B-scans,  $W(z, j)$  is an intensity mask defined as

$$W(z, j) = \begin{cases} 1 & : \overline{E_{out}}(z, j+1)\overline{E_{out}}(z, j)^* > \varepsilon^2 \\ 0 & : \text{otherwise} \end{cases} \quad (28)$$

and  $\varepsilon^2$  is the intensity of the noise floor of an OCT image.

For the particular case of  $m = 1$ , the bulk-phase-offset-free Doppler phase shift can be defined as

$$\overline{\Delta\phi}(z, j) = \text{Arg} \left[ \overline{E_{out}}(z, j+1)\overline{E_{out}}(z, j)^* \exp(-i\phi_b(j))W(z, j) \right]. \quad (29)$$

For displaying optical coherence angiography, the squared intensity of the Doppler phase shift  $|\overline{\Delta\phi}(z, j)|^2$  is used, and this image is denoted as a power-of-Doppler-shift image.

### 3.8. Sensitivity-enhanced scattering OCT

A sensitivity-enhanced scattering OCT can be defined using the coherent composition of the matrix entries as  $I(z, j) = |\overline{E_{out}}(z, j)|^2$ .

Furthermore, with our particular measurement protocol, high-quality scattering OCT is obtained by complex-averaging  $m$  B-scans obtained at the same location on the sample as

$$\overline{I}(z, j) = \left| \sum_{j=m_0}^{m_0+m-1} \overline{E_{out}}(z, j) \exp\left(-i\Delta\varphi(z)^{(m_0, j)}\right) \right|^2 \quad (30)$$

where  $m_0$  is the starting B-scan index of the multiple B-scans and  $\Delta\varphi(z)^{(m_0, j)}$  is the global phase offset between matrices defined by Eq. (14) with substitutions of  $\mathbf{M}^{(0)}$  by  $\mathbf{E}_{out}(z, m_0)$  and  $\mathbf{M}^{(j)}$  by  $\mathbf{E}_{out}(z, j)$ . We denote the high-quality scattering OCT obtained by Eq. (30) as global-phase-corrected sensitivity-enhanced scattering OCT.

Yet another type of sensitivity-enhanced scattering OCT is defined as

$$\overline{I}'(z, j) = \left| \sum_{j=m_0}^{m_0+m-1} \overline{E_{out}}(z, j) \exp\left(-i\phi'_b(m_0, j)\right) \right|^2 \quad (31)$$

where  $\phi'_b(m_0, j)$  is the bulk phase offset between  $\overline{E_{out}}(z, m_0)$  and  $\overline{E_{out}}(z, j)$  defined as

$$\phi'_b(m_0, j) = \text{Arg} \left[ \sum_z \overline{E_{out}}(z, j)\overline{E_{out}}(z, m_0)^* \right]. \quad (32)$$

We denote this type of high-quality scattering OCT as bulk-phase-corrected sensitivity-enhanced scattering OCT.

As discussed later in Section 5.3, the global-phase-corrected and bulk-phase-corrected sensitivity-enhanced scattering OCTs provide different scattering contrast. For cases shown in Section 4, global-phase-corrected sensitivity-enhanced scattering OCT is utilized.

## 4. Results

To demonstrate the clinical potential of MC-JMT, a posterior eye of a healthy subject and a geographic atrophy patient were measured. The transversal area of 4.5 mm (horizontal)  $\times$  4.5 mm (vertical) was scanned with  $512 \times 1024$  A-scans in 6.6 seconds.

In this measurement protocol, 4 B-scans were taken at a single location and used to create a sensitivity-enhanced Doppler signal (Eq. (27)) and global-phase-corrected sensitivity-enhanced scattering OCT (Eq. (30)), where the Doppler time separation was 6.4 ms. Hence, the final number of B-scans after processing was 512.

For retardation imaging, the 4 B-scans were averaged by the adaptive Jones matrix averaging method described in Section 3.4 prior to calculating the eigenvalues. DOPU was also obtained from the averaged Jones matrix.

All protocols for measurement were approved by the Institution Review Board of University of Tsukuba. Written, informed consent was obtained prior to measurement.

#### 4.1. Jones matrix Doppler imaging

The macula and optic nerve head (ONH) of the right eye of the healthy subject were scanned by MC-JMT. Figure 3(a) shows the OCT images taken by the two BPDs in the PD detection unit. An OCT signal obtained by a single BPD contains two OCT images at different depths, which corresponds to two incident polarization states. The calibration signal exists at approximately the center of the depth field.

Figures 3(b)–3(e) represent the global-phase-corrected sensitivity-enhanced scattering OCT (b), phase retardation (c), DOPU images (d), and squared power of the Doppler phase shift (e). In the sensitivity-enhanced scattering OCT (Fig. 3(b)), retinal layers including the retinal nerve fibers layer (RNFL), ganglion cell layer (GCL), internal plexiform layer (IPL), inner nuclear layer (INL), outer plexiform layer (OPL), outer nuclear layer (ONL), external limiting membrane (ELM), junction of the inner and outer segments of the photoreceptor (IS/OS) and posterior tip of the outer segment (PT), retinal pigment epithelium (RPE), and choroid (CH) are visualized despite the relatively low sensitivity of the raw OCT image at 91.05 dB.

Among the layers, the ELM, IS/OS and PT layers exhibited hyper-scattering lines in the scattering OCT, while they showed constant phase retardation in the retardation image (Fig. 3(c)). In the DOPU image (Fig. 3(d)), the RPE appears as a low DOPU band. In the power-of-Doppler-phase-shift image (Fig. 3(e)), a retinal vessel is clearly visible. The choroid vascular layer below the RPE is also densely visualized as exhibiting random phase shift signals.

Similar aspects also appeared in the images of ONH as shown in Fig. 4. From the phase retardation image of the ONH (Fig. 4(b)), the birefringence of lamina cribrosa and sclera are clearly visualized with rapidly varying phase retardation along the depth while they are not identified in the scattering OCT or the DOPU images. In particular, the scleral canal rim at the edge of the ONH exhibits strong birefringence.

In addition to the multi-contrast images, the *en face* projection of scattering OCT and the power of Doppler phase shift are shown in Fig. 5. From the *en face* scattering OCT (Fig. 5(a)), general posterior eye structures such as a myopic conus and retinal vessels are visualized. The choroidal vessels which are located deeper in the region than the retinal vessels are not clearly visible. Conversely, the choroidal vessels are observed with enhanced contrast in the *en face* projection of the power of Doppler phase shift (Fig. 5(b)). The detail of blood vessels shown in the power-of-Doppler-phase-shift image is consistent with that of indocyanine green angiography (ICGA) shown in Fig. 5(c).

#### 4.2. Geographic atrophy

In this study, an eye of a geographic atrophy (GA) patient (72-year-old Japanese male) was examined by MC-JMT to evaluate the clinical performance of the device.

GA is an advanced form of dry AMD, and here atrophy refers to the degeneration of the RPE cells. GA is usually defined by a sharply circumscribed area of pigment epithelial atrophy through which choroidal vessels can be seen [73, 74]. The continent-shaped area appears different from the surrounding retina because of the loss of the pigmented RPE in the color fundus and fundus auto-fluorescence (FAF) images as shown in Figs. 6(a) and 6(b). The area of GA looks whiter than the surrounding area in the color fundus and appears dark in the FAF image. The enhanced visibility of the choroidal vasculature in the GA region was found in the

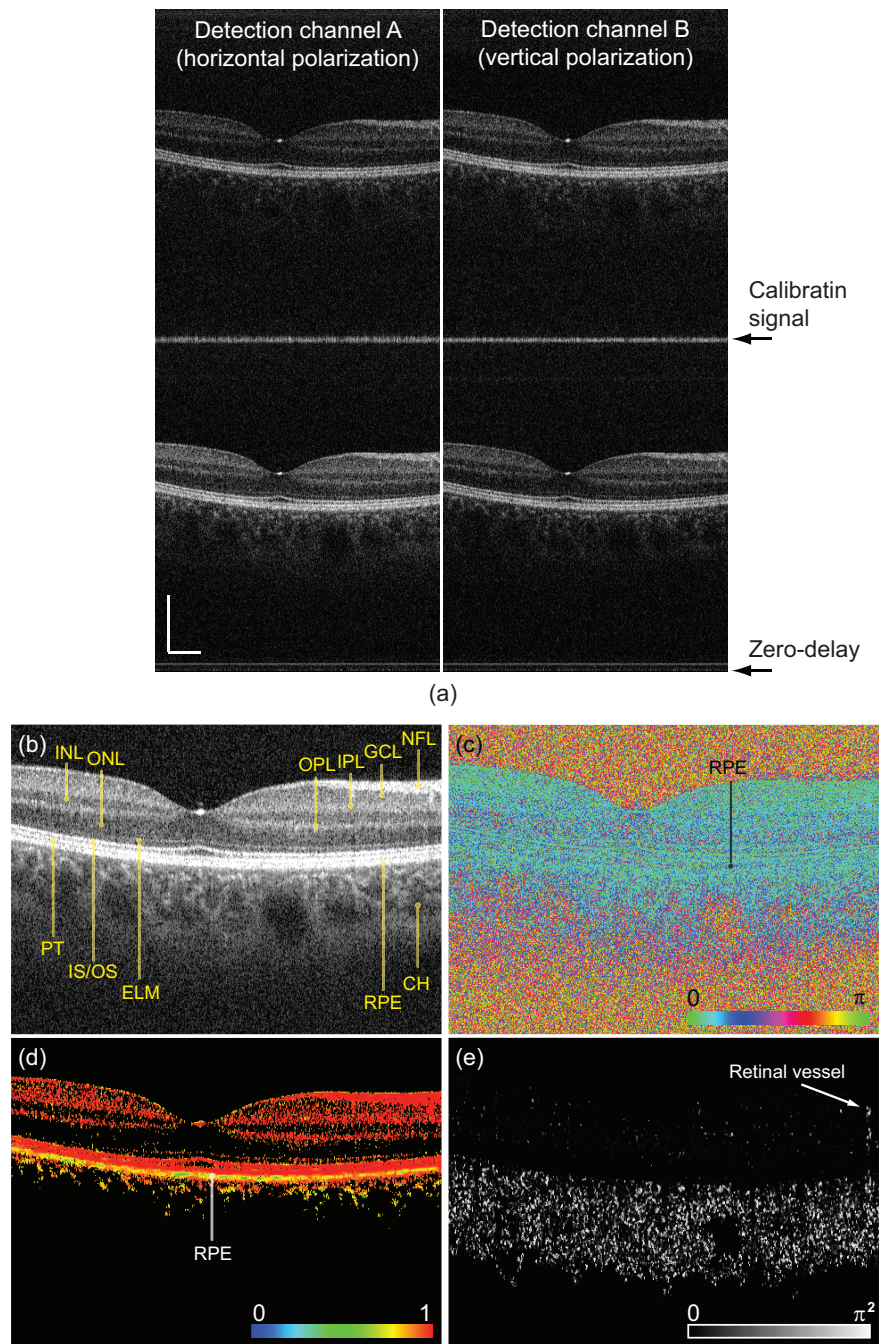


Fig. 3. MC-JMT cross-sectional images of a normal macular. (a) Raw OCT intensity images detected by detection channels of A (horizontal polarization) and B (vertical polarization) of the PD detection unit. The lower and upper images correspond to the first and second polarization state, respectively. (b) Global-phase-corrected sensitivity-enhanced scattering OCT obtained by coherent composition. (c) A phase retardation image, (d) A DOPU image, (e) power-of-Doppler-phase-shift image (e). The scale bar represents  $500 \mu\text{m} \times 500 \mu\text{m}$ .

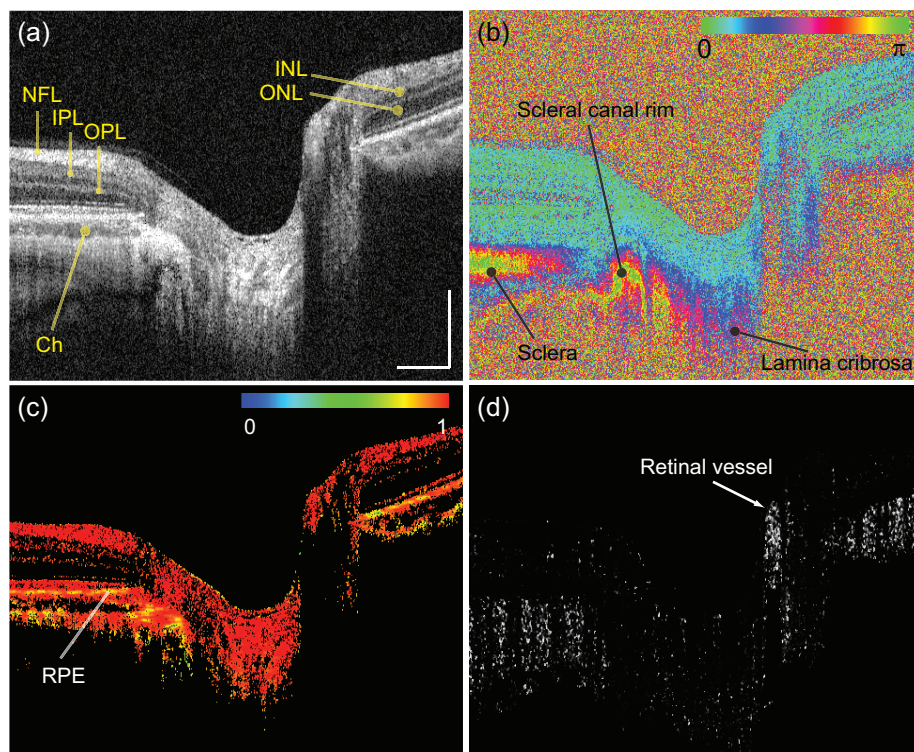


Fig. 4. MC-JMT cross-sections of a normal ONH. (a) a global-phase-corrected sensitivity-enhanced scattering OCT, (b) phase retardation, (c) DOPU, and (d) power of Doppler phase shift. The scale bar represents  $500 \mu\text{m} \times 500 \mu\text{m}$ .

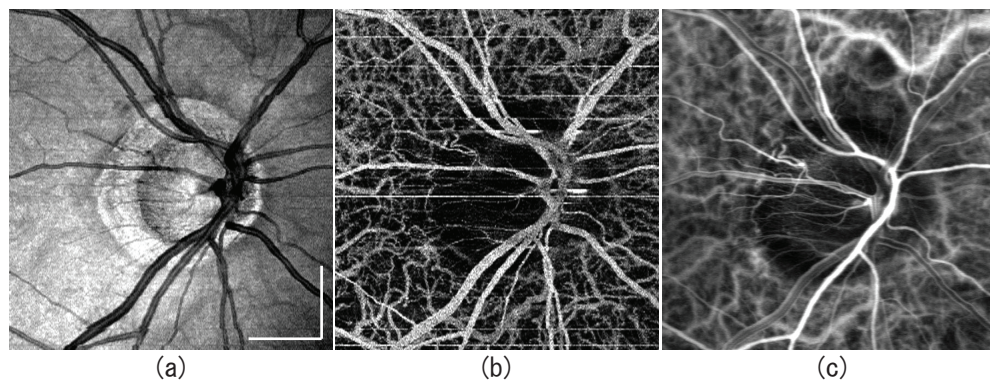


Fig. 5. *En face* projection images of (a) global-phase-corrected sensitivity-enhanced scattering OCT, (b) power of Doppler shift and (c) ICGA of an ONH. The scale bar represents  $1 \text{ mm} \times 1 \text{ mm}$ .

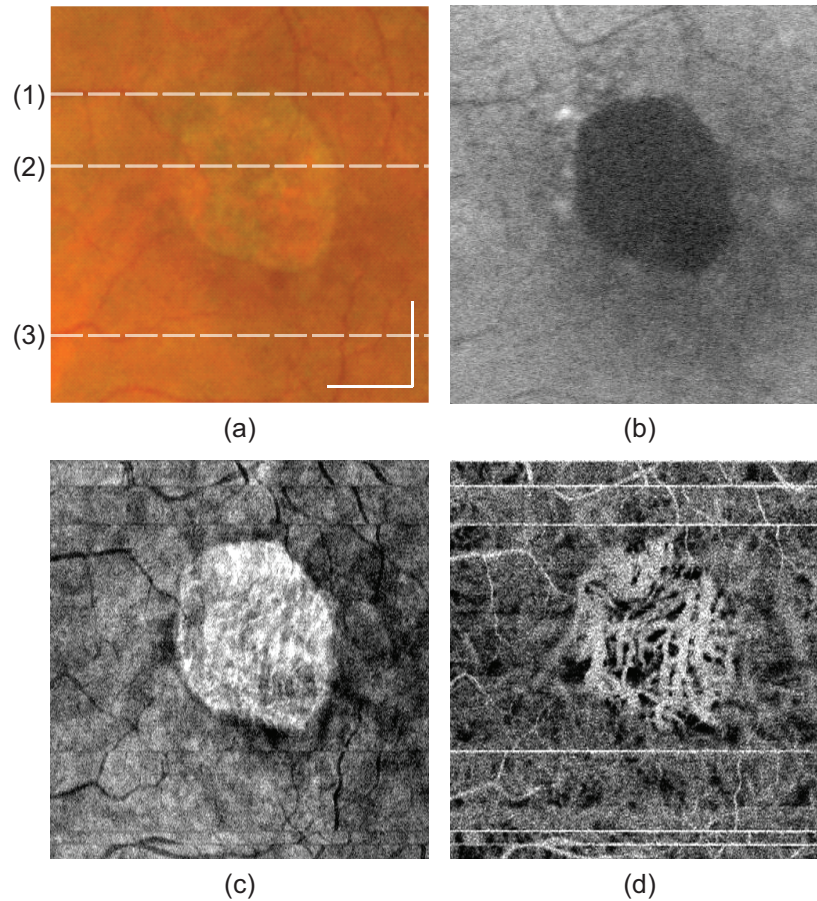


Fig. 6. *In vivo* measurement images of a GA patient; (a) fundus photograph, (b) fundus auto-fluorescence image, *en face* projection images of (c) global-phase-corrected sensitivity-enhanced scattering intensity, and (d) Doppler shift power. The scale bar indicates  $1 \text{ mm} \times 1 \text{ mm}$ .

scattering OCT as shown in Fig. 6(c), while the choroidal vasculature in this region is more clearly visible in the power-of-Doppler-shift image as shown in Fig. 6(d).

Typically, a histopathologic section of GA shows the thinning or absence of RPE, closure of the choriocapillaris, and degeneration of the overlying photoreceptors [73]. For comparison between the areas with and without GA, three representative multi-contrast B-scan images are shown in Fig. 7. Figures 7(1)–7(3) correspond to the horizontal lines (1)–(3) in Fig. 6(a), which represent cross sections of the near-edge, middle, and area outside of the GA region, respectively.

As indicated by dashed lines, the atrophic regions appeared in the scattering OCT as regions without RPE. The absence of RPE is more clearly visualized by DOPU images.

It is also noteworthy that some part of the choroid shows low DOPU values. Since melanin exists in the choroid [75], this appearance would be associated with choroidal melanin concentration.

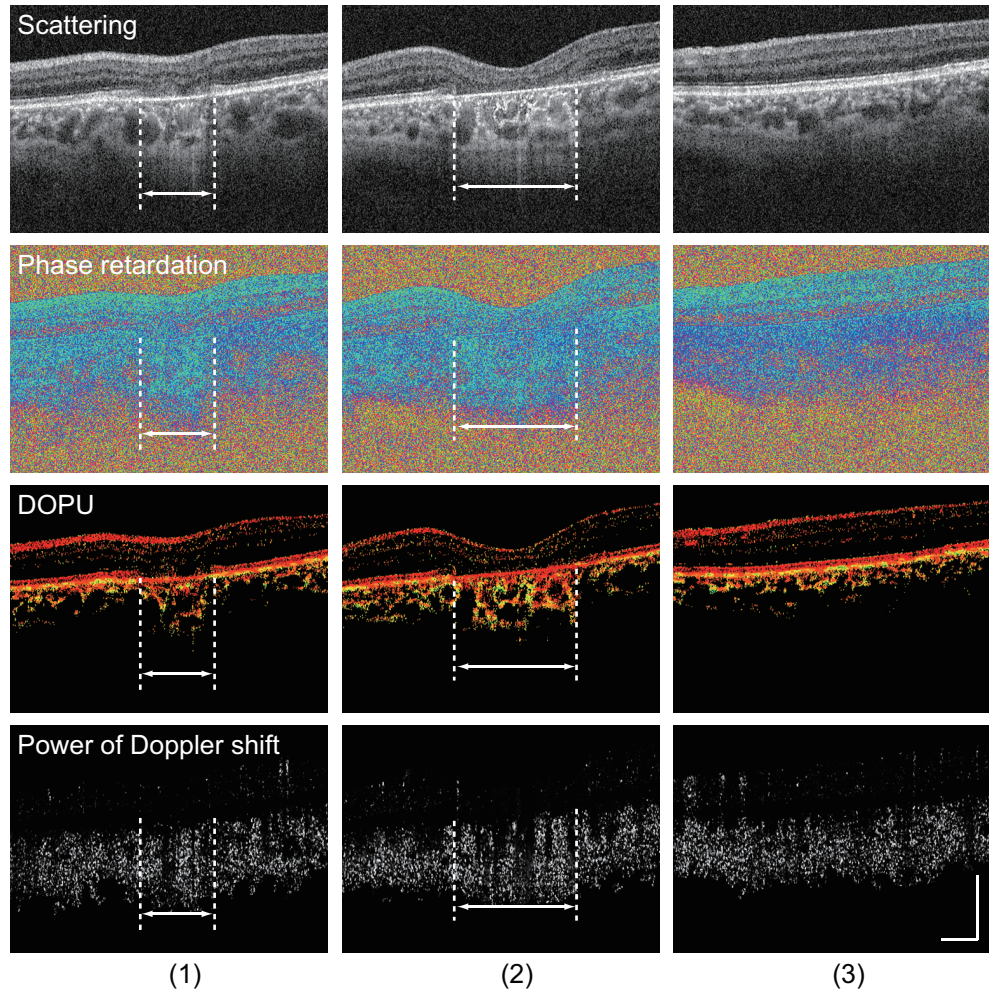


Fig. 7. Multi-contrast cross-section images of geographic atrophy. The first to the fourth rows correspond to coherent composite scattering images, phase retardation images, DOPU images, and power-of-Doppler-shift images, respectively. Columns (1)–(3) were obtained at the location indicated in Fig. 6(a). Arrows indicate the atrophic region. The scale bar indicates  $500 \mu\text{m} \times 500 \mu\text{m}$ .

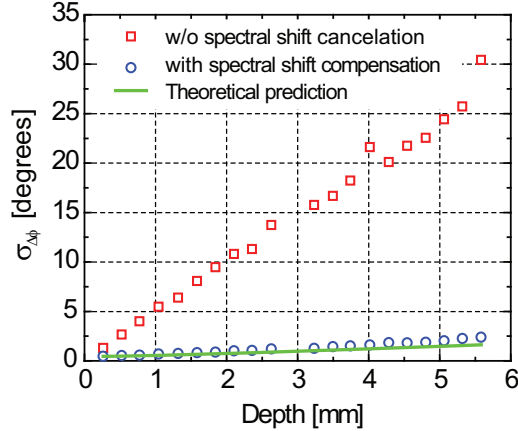


Fig. 8. Measured phase noise with ( $\circ$ ) and without ( $\square$ ) the spectral shift correction. The green line indicates the theoretical prediction.

## 5. Discussion

### 5.1. Phase stability analysis

In this section, the performance of the spectral shift correction for enhancing phase stability is examined quantitatively and qualitatively. For the phase stability test, we measured a static mirror at different depths without transversal scanning and analyzed the stability of the phase difference between adjacent A-lines. At each depth, 1024 A-lines were measured. Figure 8 shows the standard deviation of the phase differences with and without spectral shift cancellation as well as the theoretical phase noise described by [65],

$$\sigma_{\Delta\phi} = \sqrt{\left(\frac{1}{SNR_s}\right) + \left(\frac{z_s}{z_c}\right)^2 \left(\frac{1}{SNR_c}\right)} \quad (33)$$

where  $\sigma_{\Delta\phi}$  is the standard deviation of the phase difference,  $SNR_s$  and  $SNR_c$  are the SNRs of the sample, in this case a mirror, and the calibration signal.  $z_s$  and  $z_c$  are the depth positions of the sample and the calibration signal, respectively.

The result verifies enhancement of phase stability after applying the spectral shift correction. Here  $SNR_s$  was 42 dB, the roll-off measured at the depth range of 0.3 to 5.6 mm was -1.06 dB/mm, and  $SNR_c$  was 38 dB. For  $SNR_s$  of 42 dB,  $\sigma_{\Delta\phi}$  was measured to be 0.47 degree (8.16 mrad), while its theoretical prediction was 0.46 degree (8.02 mrad). This phase stability is comparable to previously published swept-source OCT [66]. Although recognizable difference between measured phase noise of 2.38 degree (41.58 mrad) and the theoretical prediction of 1.62 degree (28.34 mrad) exists at a depth of 5.58 mm, where the  $SNR_s$  was 36 dB, it is still better than the result reported by Baumann *et al.* [35] (97 mrad at 100 kHz for the  $SNR_s$  of 35 dB).

In addition to the quantitative analysis, the impact of the spectral shift correction on the fixed-pattern noise (FPN) elimination was investigated qualitatively. The FPN consists of interference signals from undesired reflection in the interferometer from the light source and cannot be removed unless the OCT signals become to be stabilized in phase, and hence is a good indicator of the phase stability of the OCT.

As shown in Fig. 9(a), severe FPN can be seen if an FPN elimination process was not applied. Although a median estimator-based FPN elimination process [76] was applied, significant FPN

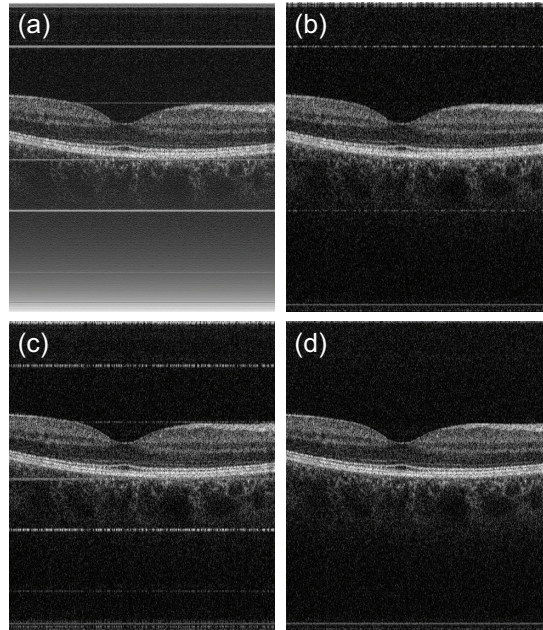


Fig. 9. OCT images of the macular of a healthy volunteer. (a) A raw image without FPN removal, (b) FPN removal without spectral shift cancellation, (c) with spectral shift cancellation and FPN removal, but no zero-padding applied. (d) FPN removal was performed after spectral shift cancellation with 1/16 pixel resolution.

still exists if spectral shift cancellation was not also applied, as shown in Fig. 9(b). The combination of the spectral shift correction with 1/16 pixel resolution and the median estimator-based FPN elimination showed elimination of almost all of the FPN, as shown in Fig. 9(d).

It is noteworthy that, without the zero-padding process required for the sub-pixel correction of the spectral shift, the FPN becomes even stronger than it is without spectral shift cancellation, as shown in Fig. 9(c). Particularly, spectral shift correction with single-pixel resolution worsened phase stability. Therefore, as mentioned in Section 3.1, a proper amount of zero-padding is essential.

## 5.2. Advantages of the phase stabilization process

The proposed phase stabilization process is based on the cross-correlation of the calibration signals that originated from general characteristics of the PBS and systematic features of the MC-JMT system. Because of the origin and location of the calibration signal, this method has several advantages over others recently reported [35, 66].

First, no specific optical component that extracts light from the interferometer, such as a coupler, is required. And hence there is no additional optical loss. This also makes the system simple and cost-efficient. Second, the calibration signal does not reduce the depth measurement range, because it appears at exactly the zero-delay point of the OCT image corresponding to the delayed polarization component. In addition, the depth location of the calibration signal does not depend on the path length of the calibration mirror arm. This further eases the optical and mechanical design of the OCT scanner, especially for applications in which the reference path length frequently alters to adjust to that of a sample arm, such as in posterior eye imaging. It should be noted that the path length difference between the 80:20 coupler to the calibration

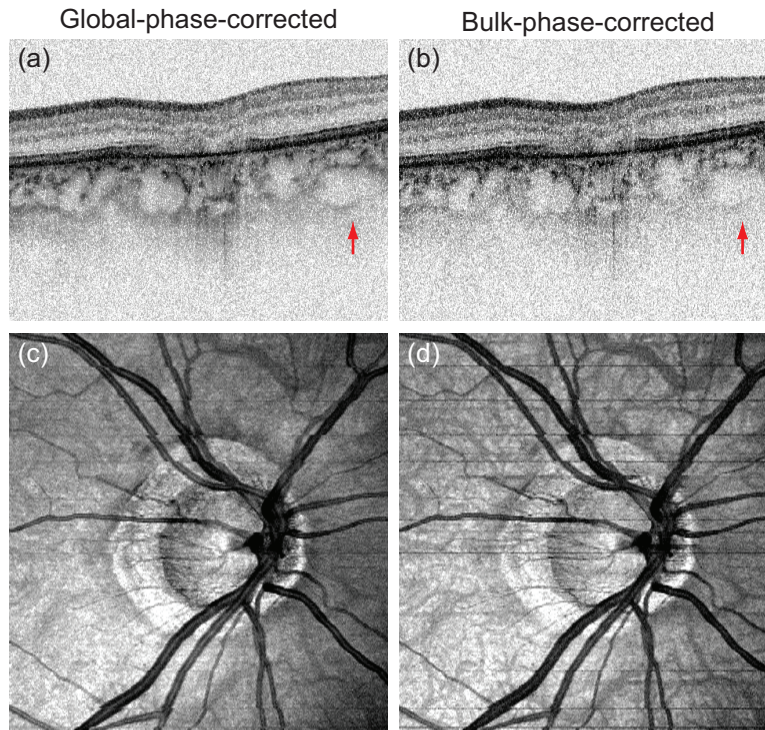


Fig. 10. The comparison between global- and bulk- phase-corrected sensitivity-enhanced scattering OCTs. (a) and (c) are a B-scan and *en face* projection of sensitivity-enhanced OCTs with global-phase correction, and (b) and (d) are those with bulk-phase correction.

mirror and the coupler to the retina should be more than the full depth measurement range that covers the depth ranges of input state-1 and -2. Otherwise the interference signal between the light from calibration mirror and the reference appears as an FPN and overlaps with the OCT image.

In addition, in comparison to a fully numerical method [67] used in our previous MC-JMT [60], the overall processes are simplified and performance is stable.

It would be fair to declare the relatively long computational time of the phase stabilization process. The current implementation is in LabVIEW 2011 on a 64-bit Windows 7 PC with an Intel core i7 950 3.07GHz CPU, and it takes around 27 minutes for a single volume consisting of  $512 \times 1024$  A-scans. Since the phase stabilizations of each A-line are independent to each other, the process can be highly parallelized by using a GPU or multiple CPU cores. So the possible parallel processing would enable sufficiently high-speed phase stabilization.

Finally, the high accuracy and effectiveness of the proposed method, as verified in the previous sections, provides a high reliability to the system for clinical applications.

### 5.3. Global-phase-corrected and bulk-phase-corrected sensitivity-enhanced scattering OCT

The global- and bulk- phase-corrected sensitivity-enhanced scattering OCTs defined in Section 3.8 provide different scattering contrasts.

Figures 10(a) and 10(b) are the examples of sensitivity-enhanced B-scans of the GA eye presented in Section 4.2. Figure 10(a) is obtained with a global-phase-corrected while Fig. 10(b) is obtained with a bulk-phase correction. In the global-phase-corrected image, the lumens of large

choroidal vessels appear with more-hyper-scattering than those in the bulk-phase-corrected image.

This difference is explained by the difference in the phase estimation methods. Namely, the global phase is estimated in point-wise, while the bulk phase is estimated in A-line-wise. Therefore the bulk-phase correction corrects a constant phase offset of each A-line, where the constant phase offset, in general, is occurred by a bulk motion of the sample and is a phase offset at the region of a static tissue. And hence, the bulk-phase correction can enhance the OCT signal at the static tissue but cannot enhance the OCT signal at regions with a localized motion, such as a region with blood flow.

On the other hand, global-phase correction corrects any phase offset including those occurred by a bulk motion and also by a localized motion. As a result, the global-phase correction enhances the OCT signals both at the static tissue and at the region with blood flow. This difference between the two phase correction methods resulted in the different contrasts of choroidal vessels.

Similarly, the global-phase correction also corrects phase offset occurred by shadowing of Doppler shift of the blood flow. This results in more hyper scattering signals at the region beneath large choroidal vessels in the global-phase-corrected image than the bulk-phase-corrected image as exemplified by an arrow in Figs. 10(a) and 10(b).

Because the signal degradation occurred by the blood flow is larger in the bulk-phase-corrected image, the choroidal vessels are more clearly appeared in the *en face* projection of bulk-phase-corrected sensitivity-enhanced scattering OCT than that of global-phase-corrected OCT. Figures 10(c) and 10(d) show an ONH of the subject presented in Section 4.1 obtained with a global-phase correction and bulk-phase correction, respectively. The bulk-phase-corrected image revealed finer details of the choroidal vessels with higher contrast than the global-phase-corrected image. On the other hand, the scattering property of the tissue would be more easily evaluated with the global-phase-corrected image. Note that Figs. 10(c) and 10(d) are displayed with a gray-color-map while Figs. 10(a) and 10(b) are displayed with an inverted-gray-color-map.

Since the phase-offset occurred by quick eye motion reduces the signal intensity of the sensitivity-enhanced OCT, the quick eye motion creates a dark horizontal line artifact in the *en face* projection as shown in Fig. 10(d). As exemplified by the vessel contrast, the global-phase correction has higher ability to correct the phase-offset than the bulk-phase correction. And hence the contrast of the dark horizontal line artifacts in the *en face* image created with the global-phase correction (Fig. 10(c)) is significantly less than that with bulk-phase correction (Fig. 10(d)).

#### 5.4. Effect of practical factors in JMT measurement

In this discussion, we present the fundamental robustness of the JMT method. As discussed in Section 3.2, the relationship between incident and output light in an ideal JMT is described by Eq. (7).

In a practical system, we should consider several additional factors. By accounting for these factors and by substituting  $\mathbf{J}_{all}(z) = \mathbf{J}_{out}\mathbf{J}_s(z)\mathbf{J}_{in}$ , Eq. (7) is modified to

$$\mathbf{E}_{out}(z) = \eta \mathbf{X}' \mathbf{R} \rho \mathbf{J}_{out} \mathbf{J}_s(z) \mathbf{J}_{in} \mathbf{X} f(\mathbf{X} \mathbf{E}_{in}) \quad (34)$$

where  $\mathbf{X}$  is a matrix representing the imperfection of the PBS in the polarization delay unit. As we used it to generate the calibration signal, there is a significant amount of polarization cross-talk in the PBS. The off-diagonal entries of  $\mathbf{X}$  account for the cross-talk and the diagonal entries represent the transmittance and reflectance of the horizontally and vertically polarized light.  $f(\cdot)$  is a function which represents the delay between two incident polarization states gen-

erated by the polarization delay unit.  $\mathbf{R}$  represents interference with the reference beams and is  $\mathbf{R} = \begin{bmatrix} H_{ref}^* & 0 \\ 0 & V_{ref}^* \end{bmatrix}$  where  $H_{ref}^*$  and  $V_{ref}^*$  are the complex conjugates of the field amplitudes of the reference beam with horizontal and vertical polarization states.  $\rho$  is a rotation matrix representing the relative rotation between the polarization delay unit and the PD detection unit.  $\mathbf{X}'$  represents the imperfection of the PBS in the PD detection unit, similar to that of the polarization delay unit  $\mathbf{X}$ . Finally,  $\eta$  represents the detection efficiency of the two BPDs in the polarization delay unit as  $\eta = [\eta_A \ 0; \ 0 \ \eta_B]$ , where  $\eta_A$  and  $\eta_B$  are the detection efficiencies of the two BPDs.

Although  $\mathbf{E}_{out}(z)$  is affected, these practical factors do not affect the phase retardation measurement. In JMT, a similar matrix of  $\mathbf{J}_s(z)$  is obtained by Eq. (10). By substituting Eq. (34) for Eq. (10), we found

$$\mathbf{E}_{out}(z)\mathbf{E}_{out}(z_0)^{-1} = \eta \mathbf{X}' \mathbf{R} \rho \mathbf{J}_{out} \mathbf{J}_s(z) \mathbf{J}_{out}^{-1} \rho^{-1} \mathbf{R}^{-1} \mathbf{X}'^{-1} \eta^{-1}. \quad (35)$$

It is evident that the right-hand side of this equation retains its similarity to  $\mathbf{J}_s(z)$ . Hence all the practical factors discussed in this section do not significantly affect the JMT measurement.

## 6. Conclusion

In this study, an advanced MC-JMT system based on a passive polarization delay at 1- $\mu\text{m}$  wavelength was presented. Because of the accurate spectral shift correction method based on cross-correlation of the calibration signal originated from the general characteristics of PBS, we achieved a highly phase-stabilized system.

A theory of JMT which integrated polarization measurement, Doppler Measurement, and scattering measurement was presented. Owing to this new theory and high phase stability, highly-sensitive Doppler OCT and sensitivity-enhanced scattering OCT were demonstrated.

*In vivo* measurements of a healthy and pathologic eye were demonstrated. The Doppler image revealed small vessels invisible in the OCT intensity image, while the phase retardation and DOPU image demonstrated tissue-selective visualization of the human retina and choroid. These results indicate the clinical utility of MC-JMT.

## Acknowledgment

This research was supported in part by the Japan Society for the Promotion of Science (JSPS) (KAKENHI 11J01600). Myeong Jin Ju is partially supported by a University of British Columbia Four Year Fellowship and Young-Joo Hong is supported by JSPS.